FULL PAPER

Theranostics

NANO · MICRO
small
www.small-journal.com

Check for updates

Cellular Internalization–Induced Aggregation of Porous Silicon Nanoparticles for Ultrasound Imaging and Protein-Mediated Protection of Stem Cells

Shengcai Qi, Pengfei Zhang, Ming Ma,* Minghua Yao, Jinjin Wu, Ermei Mäkilä, Jarno Salonen, Heikki Ruskoaho, Yuanzhi Xu, Hélder A. Santos,* and Hongbo Zhang*

Nanotechnology employs multifunctional engineered materials in the nanoscale range that provides many opportunities for translational stem cell research and therapy. Here, a cell-penetrating peptide (virus-1 transactivator of transcription)–conjugated, porous silicon nanoparticle (TPSi NP) loaded with the Wnt3a protein to increase both the cell survival rate and the delivery precision of stem cell transplantation via a combinational theranostic strategy is presented. The TPSi NP with a pore size of 10.7 nm and inorganic framework enables high-efficiency loading of Wnt3a, prolongs Wnt3a release, and increases antioxidative stress activity in the labeled mesenchymal stem cells (MSCs), which are highly beneficial properties for cell protection in stem cell therapy for myocardial infarction. It is confirmed that the intracellular aggregation of TPSi NPs can highly amplify the acoustic scattering of the labeled MSCs, resulting in a 2.3-fold increase in the ultrasound (US) signal compared with that of unlabeled MSCs. The translational potential of the designed nanoagent for real-time US imaging–guided stem cell transplantation is confirmed via intramyocardial injection of labeled MSCs in a nude mouse model. It is proposed that the intracellular aggregation of protein drug–loaded TPSi NPs could be a simple but robust strategy for improving the therapeutic effect of stem cell therapy.

1. Introduction

The technique of stem cell therapy holds great potential for treating a wide range of diseases, including cancer, skin diseases, and cardiovascular diseases.[1] In particular, stem cell–based transplantation has become a promising therapeutic strategy for the regeneration of injured heart, owing to its ability to stimulate cardiac regeneration potential and reconstitute the cardiomyocyte loss.[1f] For therapeutic purposes, stem cells must be precisely delivered to the site of action and be able to sustainably secrete active factors or differentiate into specific cell lines in a relatively short period of time; however, both of these features are still unsatisfactory at the current stage and limit the progress of stem cell therapies.[2]

To improve the therapeutic accuracy and efficiency of cardiac regeneration, multiple imaging techniques, such as magnetic resonance imaging, photoacoustic imaging, and bioluminescence imaging,

Dr. S. Qi, J. Wu, Prof. Y. Xu
Department of Stomatology
Shanghai Tenth People's Hospital
Tongji University School of Medicine
Shanghai 200072, China

Dr. P. Zhang
The Key Laboratory of Cardiovascular Remodeling
and Function Research of Chinese Ministry of Education
Department of Cardiology
Qilu Hospital of Shandong University
Jinan, Shandong 250012, China

Prof. M. Ma
State Key Laboratory of High Performance Ceramics
and Superfine Microstructures
Shanghai Institute of Ceramics
Chinese Academy of Sciences
Shanghai 200050, China
E-mail: mma@mail.sic.ac.cn

Prof. M. Ma, Dr. M. Yao, Prof. H. Zhang
Department of Pharmaceutical Science Laboratory
Åbo Akademi University
Turku 20520, Finland
E-mail: hongbo.zhang@abo.fi

E. Mäkilä, Prof. J. Salonen
Department of Physics and Astronomy
University of Turku
Turku 20014, Finland

Prof. H. Ruskoaho, Prof. H. A. Santos
Drug Research Program
Faculty of Pharmacy
University of Helsinki
FI-00014 Helsinki, Finland
E-mail: helder.santos@helsinki.fi

ADVANCED
SCIENCE NEWS
www.advancedsciencenews.com

NANO · MICRO
small
www.small-journal.com

have been used as promising methods for stem cell labeling to guide cell delivery and to determine the survival and local activity of stem cells in implanted site.[3] Among different imaging techniques, ultrasound (US) imaging is more feasible for future clinical applications, because it is noninvasive, cost-effective, widely available, portable, and allows molecular imaging and real-time guided imaging without any ionizing radiation effect.[4] One major approach is to label stem cells with US contrast agents to achieve enhanced imaging of cells.[5] Although different types of gas-filled microbubbles can be used as contrast agents to increase echocardiography signals, unfortunately, the intrinsic poor structural stability (lifetime of 5–12 min) and micrometer-scale particle size limit their applications in cell labeling and monitoring.[6]

To employ US-enhanced imaging with high stability and sensitivity, much effort has been focused on the design and fabrication of rigid inorganic nanoparticles (NPs) with relatively high structural stability and echogenic properties.[7] Recently, silica NP–based US contrast agents have received intensive interest, because of their low toxicity, adjustable structure and particle size, and their high performance in acoustic scattering at high US frequencies.[8] For example, Zhang et al. systematically investigated the effect of silica NP structure on the acoustic properties and showed that rattle-shaped mesoporous silica NPs exhibit superior US imaging capability compared with solid- and hollow-structured NPs.[9] Additionally, Jokerst and coworkers confirmed the feasibility of US imaging–guided delivery of stem cells into the myocardium with the use of a silica NP–based labeling agent.[10] However, the biodegradability and metabolism of silica NPs in biological body is still controversial, limiting their future clinical application.[11]

In addition, mesenchymal stem cells (MSCs), which are generally extracted from animal or human sources, have been widely investigated in basic and preclinical research for treating different injuries and diseases.[12] Although the safety of MSC therapies has been consistently reported, their efficacy remains more elusive. In particular, their low survival rate in infarcted tissue (such as myocardium, liver, and brain) is a major limitation for clinical translation.[13] In particular, the reactive oxygen species (ROS) generated at the ischemic site of injury could dramatically induce the loss of transplanted MSCs.[14] Thus, a powerful strategy that can manipulate MSCs to significantly attenuate ROS-induced damage and thereby promote MSC survival and differentiation is urgently needed for both preclinical research and future clinical application of stem cell therapy.

As a promising alternative, we propose replacing silica-based NPs with porous silicon nanoparticles (PSi NPs) to act as US contrast agents for cellular labeling and US
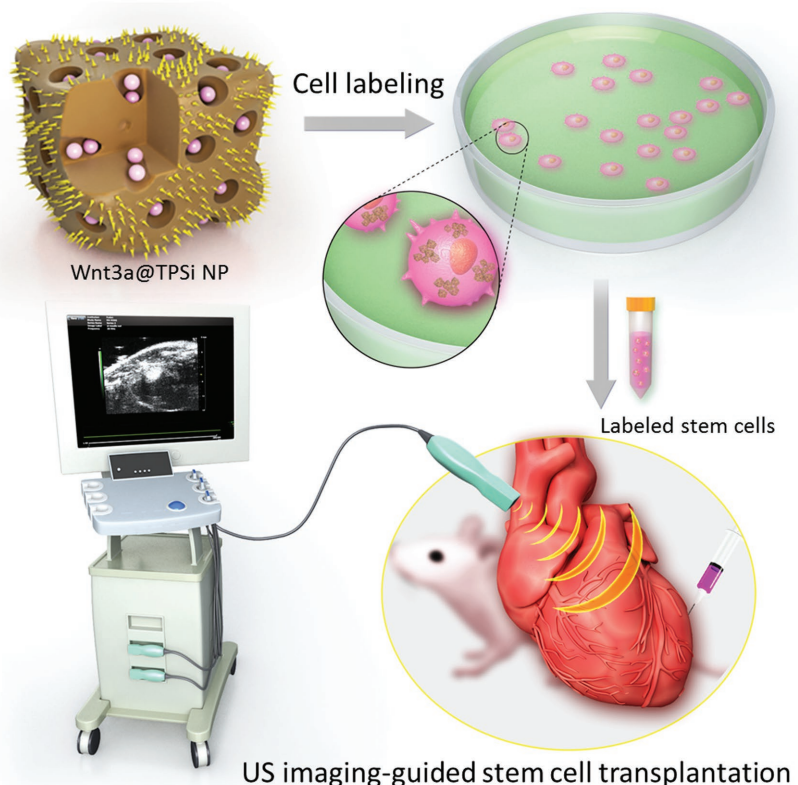
Scheme 1. Schematic illustration of stem cells labeled with Wnt3a protein–loaded TPSi NPs injected intramyocardially into nude mice under US imaging guidance.

imaging–guided stem cell transplantation (shown in **Scheme 1**). PSi materials have received wide attention in the field of biomedical nanotechnology, because these NPs are more biodegradable than silica NPs.[15] The porous structure of PSi NP is produced by electrochemical etching, which enables the tailored manipulation of pore size and pore volume for a high drug-loading capacity.[16] Therefore, we investigated the possibility of surface modification of PSi NPs with virus-1 transactivator of transcription (TAT) peptide[17] to create a dual-functional enhanced imaging/protein drug delivery system with great potential for clinical translation (the obtained nanoparticle is denoted as TPSi NP). The possible cytotoxicity, in vivo safety, and biodegradability of TPSi NP were systemically studied in this study. In addition, a typical multifunctional protein, Wnt3a, was used to evaluate the loading efficiency and release behavior of protein drug–loaded TPSi NP. Importantly, previous reports have confirmed the protective effect of Wnt3a against oxidative stress in cells through the Wnt/β-catenin signaling pathway.[18] However, since this protein drug generally shows poor structural stability and low delivery efficacy, it has been of limited use for stem cell therapy. Therefore, another important purpose of this study is to investigate the effect of Wnt3a-loaded TPSi NP on the cell protective activity for the labeled stem cells. This integrated technique presents concurrent US contrast imaging and protein drug delivery within one TPSi NP, which could offer remarkable advantages for future cardiac stem cell therapy.

2. Results and Discussion

2.1. TPSi NP Synthesis and Characterization

The PSi NPs were constructed to have fluorescence and enhanced internalization into MSCs. A sequential fabrication process including electrochemical anodization, thermal carbonization, and surface modification with aminosilanes was conducted to obtain PSi NPs containing amine groups. Furthermore, the particle surface was chemically decorated with fluorescein isothiocyanate (FITC)–conjugated TAT peptide (TAT-FITC) by an esterification reaction to promote the cellular internalization of the NPs.[19] The TPSi NPs exhibit a porous structure as observed in transmission electron microscopy (TEM) images (**Figure** 1A,B). The profile from electron energy loss spectroscopy (EELS) mapping of particles in a TEM system confirmed that the main component of the particle product is Si (Figure 1B). Additionally, scanning electron microscopy (SEM) analysis of the obtained NPs showed a pore structure with an average pore size of ≈10.7 nm, as measured by ImageJ software (Figure 1C; Figure S1, Supporting Information). Meanwhile, the N_2 sorption profile shows that the particle exhibits specific surface area of 352 m^2 g^{-1} and a total pore volume of 0.76 cm^3 g^{-1} (Figure 1D). In addition, the successful conjugation of TAT-FITC peptide onto the surface of the TPSi NPs was confirmed by UV–vis spectroscopy. As indicated in Figure 1E, a significant decrease in the characteristic absorbance peak of TAT-FITC in solution was found after centrifugation of the NPs. Thus, it was calculated that ≈71 mmol of peptide was conjugated per gram of TPSi NPs. We also found

that the conjugation of TAT-FITC on TPSi NPs was quite stable, as no obvious optical absorption at 495 nm (the characteristic absorption of the released TAT-FITC) was observed for TAT-FITC-conjugated TPSi NPs after immersion in ethanol for 24 h (Figure S2, Supporting Information). Furthermore, as dynamic light scattering (DLS) result shows (Figure 1F), the TAT conjugation can alter the hydrodynamic size distribution of TPSi NPs in phosphate-buffered solution (PBS), owing to the chemical property change of particle surface. The hydrodynamic size increases from ≈314.8 nm (unconjugated) to ≈351.8 nm after the conjugation reaction.

2.2. Cellular Labeling

After coincubation of MSCs with functionalized TPSi NPs at a concentration of 40 µg mL^{-1} for 4 h, the cells were washed to remove the unbound TPSi NPs. Using fluorescence microscopy (**Figure** 2A–C) and confocal laser scanning microscopy (CLSM; Figure S3, Supporting Information), we observed that a considerable number of TPSi NPs localized to the MSCs. TEM imaging of the labeled MSCs revealed that the TPSi NPs were mainly localized in the cytoplasm and formed clusters with sizes ranging from 1 to 2 µm (Figure 2D,E; Figure S4, Supporting Information). Additionally, energy-dispersive X-ray spectroscopy (EDS) spectra indicated the existence of the element Si within MSCs. Furthermore, the Si content inside the cells after MSC labeling was measured by inductively coupled plasma atomic emission spectroscopy (ICP-AES), and the result showed that ≈78.8% of TPSi NPs were localized in the cell
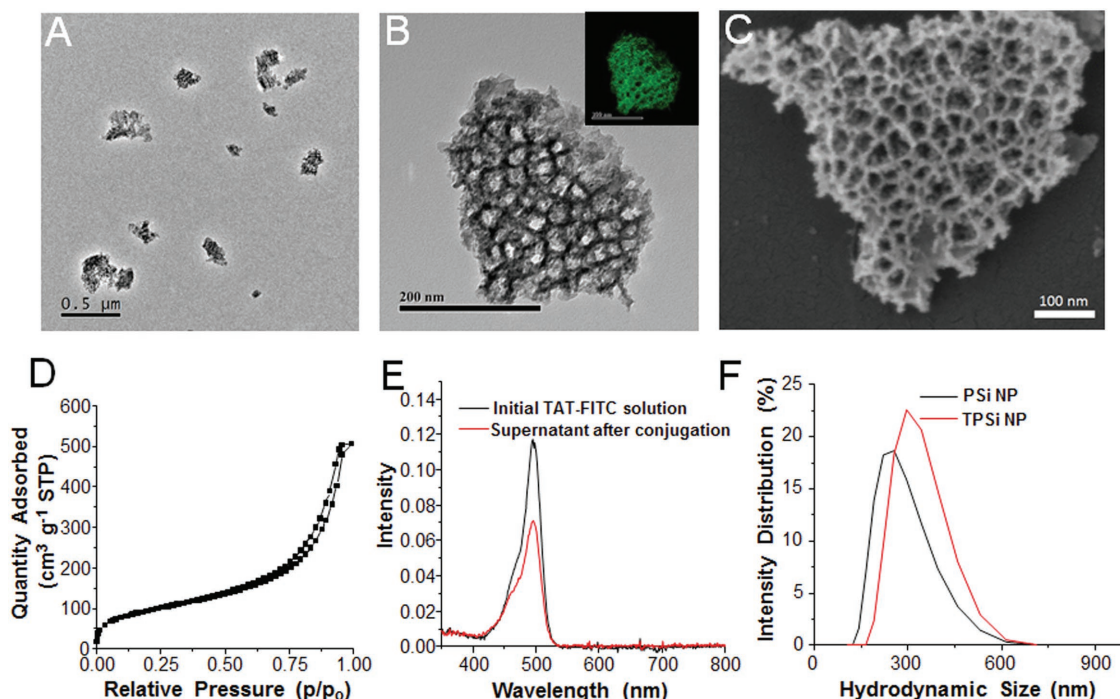
Figure 1. A,B) TEM images of TPSi NPs at different magnifications. Inset image in part (B): EELS mapping of the element Si in TPSi NPs. C) SEM image of TPSi NPs. D) N_2 adsorption–desorption isotherm for TPSi NPs. E) UV–vis absorption spectra of the initial TAT-FITC solution (black line) and the supernatant containing unbound TAT-FITC after sequential chemical conjugation of TAT-FITC and centrifugation of NPs (red line). F) Hydrodynamic size distribution curves of PSi NP and TPSi NP in PBS.
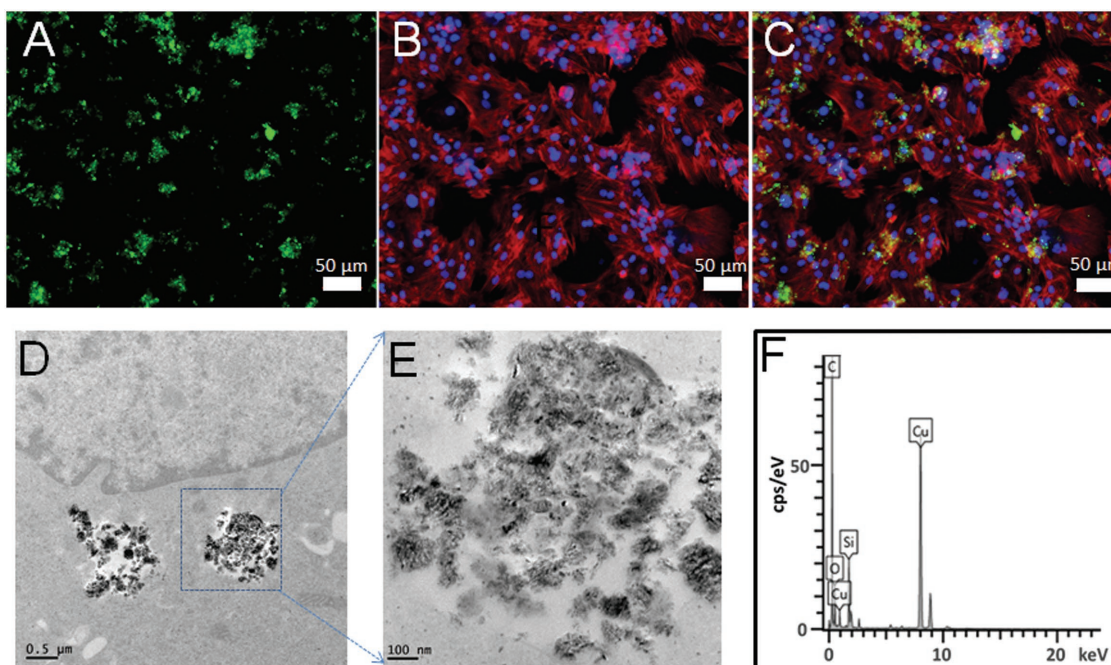
Figure 2. Fluorescence microscopy images of TPSi NP–labeled MSCs. A) TPSi NPs with green fluorescence, B) merged image of 4′,6-diamidino-2-phenylindole-stained nuclei and tetramethylrhodamine isothiocyanate–phalloidin-stained F-actin, and C) merged image of TPSi NPs, nuclei, and F-actin. D,E) TEM images of TPSi NPs within MSCs. F) EDS spectra of the intracellular region containing porous NPs.

(Figure S5, Supporting Information). However, only 52.7% of TAT-unconjugated PSi NPs were internalized by MSCs under the same conditions (Figure S5, Supporting Information). The result reveals a high labeling efficiency of PSi NP resulting from the TAT conjugation.

2.3. TPSi NP Biodegradation

The biodegradation behavior and the structural evolution of TPSi NPs in MSCs were further studied. MSCs were harvested and fixed in ultrathin sections for TEM observation after incubation with TPSi NPs to label the MSCs (TPSi NP concentration of 40 µg mL^{-1}) for different periods (1, 8, and 16 d). As shown in **Figure 3**A, the particle diameter above 100 nm and the obvious porous structure were still present after 1 d. However, the extended coincubation for 8 d resulted in a dramatic decrease in particle size and a less organized pore structure for the TPSi NPs, indicating that significant biodegradation of TPSi NPs occurred in the MSCs. Furthermore, distinct changes in particle morphology and only several spherical objects with particle sizes below 10 nm were observed after incubation for 16 d. Collectively, the above results confirmed the feasibility of intracellular TPSi NP degradation.

To further understand the mechanism by which the cellular environment influences the biodegradation of TPSi NPs, the TPSi NPs were placed in PBS at three representative pH values (5.4, 7.4, and 8.4) to investigate the corresponding Si ion release rate. The free Si ions were quantitatively measured after different durations (1–16 d) by ICP-AES. As shown in Figure 3B, gradual silicate ion leaching of TPSi NPs into the solution was observed when placed in pH 7.4 PBS, and the

cumulative release proportion reached nearly 37% after 16 d. Additionally, only debris-like silicon fragments were observed in the TEM image (Figure 3C). In contrast, the silicate ion release increased significantly at pH 8.4, with ≈84% of silicate ions leaching into solution in 16 d (Figure 3B), which indicates that the basic environment has a positive effect on the biodegradation of TPSi NPs. In contrast to the TPSi NPs in both neutral and alkaline conditions, the TPSi NPs maintained their large pore structure in the weakly acidic solution (pH 5.4) as shown in Figure 3D and Figure S6 in the Supporting Information, and only ≈5% of silicate ions were released within 16 d. The above results confirmed that the hydroxide ions existing in stem cells may be the main factor that contributes to the silicon degradation.[15e,20]

2.4. Effect of TPSi NP Labeling on MSC Survival and Differentiation

The cytotoxicity of TPSi NPs at different concentrations (0, 6.25, 12.5, 25, 50, 100, and 200 µg mL^{-1}) against MSCs was first evaluated to confirm the feasibility of TPSi NPs for biological applications. After MSCs were cocultured with different concentrations of TPSi NPs for 48 h, cell viability was determined by both the Cell Counting Kit-8 (CCK-8) and the lactate dehydrogenase (LDH) assays (**Figure 4**A,B). The results suggest that the TPSi NPs had no adverse effect on the survival of MSCs.

MSCs possess the capability to differentiate into multiple cell types, including adipocytes, osteoblasts, and chondrocytes.[21] When TPSi NPs are applied for intracellular labeling of MSCs, it is necessary to evaluate their potential adverse effects on the

**ADVANCED
SCIENCE NEWS**
www.advancedsciencenews.com

NANO · MICRO
small
www.small-journal.com
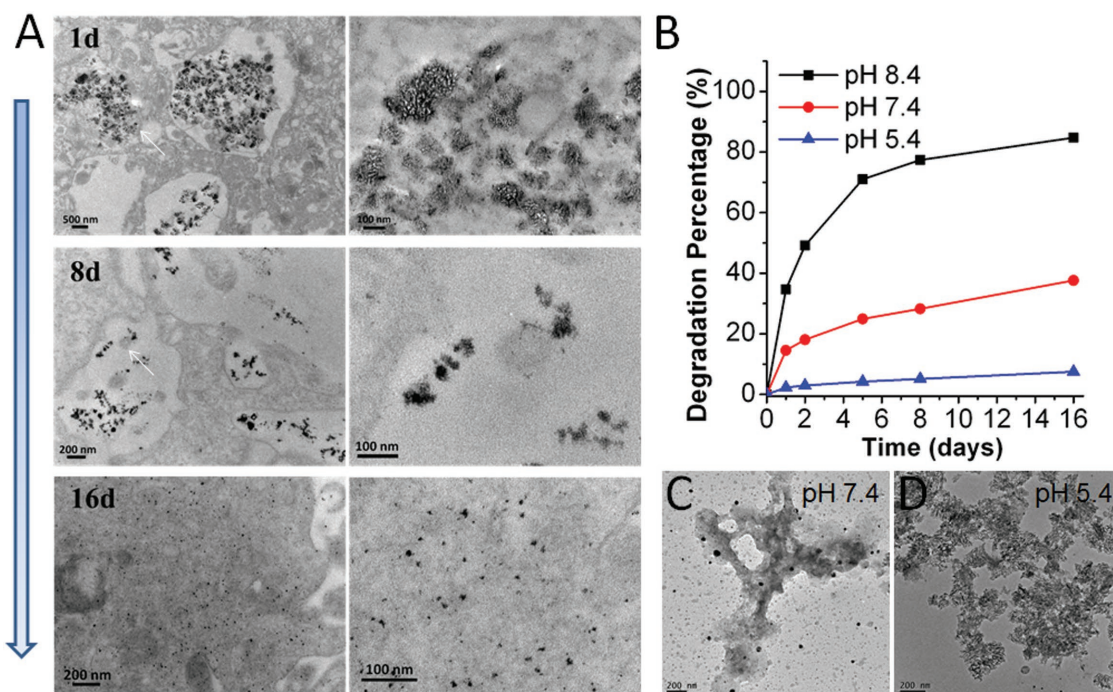
Figure 3. A) TEM images of randomly selected MSCs containing TPSi NPs after coincubation for 1, 8, and 16 d. The right panel shows the magnified image of a representative region (as indicated by the white arrow) in the left panel. B) Silicate release percentages of TPSi NPs after being immersed in PBS with different pH values (5.4, 7.4, and 8.4) for different time periods. TEM images of TPSi NPs after being immersed in C) pH 7.4 and D) pH 5.4 PBS for 16 d.

differentiation capability of MSCs. First, the effects of TPSi NPs at different concentrations (0, 40, 60, and 80 µg mL^{-1}) on the induction of MSCs to myocyte-like cells were evaluated. The bone morphogenetic protein-2 (BMP-2) and fibroblast growth factor-4 (FGF-4) were used to stimulate the MSC differentiation.[22] After treatment for 2 weeks, stretching pseudopodia and cell cluster formation were observed for each cell sample with and without pretreatment by TPSi NPs. The expression of GATA-4 and cardiac troponin I (cTnI) in each group was measured, which serve as specific markers of cardiomyocyte-like cells.[22a] As shown in Figure 4C and Figure S7 in the Supporting Information, no significant difference in the GATA-4 expression was observed in each induction group no matter pretreated with TPSi NPs (1.06 ± 0.16, 1.17 ± 0.17, and 0.93 ± 0.05 for 40, 60, and 80 µg mL^{-1}, respectively) or not (1.03 ± 0.19). In addition, their cTnI expression, as reflected by green fluorescence, was visually detected by CLSM, as indicated in Figure 4D. The mean fluorescence levels measured by flow cytometry were 45.82 ± 2.15, 42.14 ± 1.64, and 38.56 ± 1.32 for MSCs without and with pretreatment with TPSi NPs (40 and 60 µg mL^{-1}), respectively, which differed from each other nonsignificantly ($P > 0.05$). In comparison, the fluorescence level decreased slightly to 28.84 ± 1.15 when the TPSi NP concentration was 80 µg mL^{-1}. In addition, the proportion of cTnI-positive cells was lower when pretreated with such high TPSi NP concentration (80 µg mL^{-1}) than that without TPSi NP pretreatment (68.45 ± 3.65% vs 88.88 ± 1.21%, $P < 0.05$, Figure 4E). These results indicate that the TPSi NPs at the concentration above 80 µg mL^{-1} may induce adverse effect to the cardiomyogenic differentiation of MSCs. Overall, our result demonstrated

that TPSi NPs at concentrations lower than 60 µg mL^{-1} exert a negligible effect on the induction of cardiomyocyte-like cells by BMP-2 and FGF-4.

Furthermore, three other typical in vitro differentiation assays (adipogenic, osteogenic, and chondrogenic) of MSCs were conducted with and without pretreatment with TPSi NPs (particle concentration: 100 µg mL^{-1}). The adipogenic differentiation assay showed that intracellular lipid vesicles formed for both TPSi NP–treated MSCs and untreated MSCs after adipogenic induction (Figure S8A, Supporting Information). Additionally, the quantification of the Oil Red O–stained cells shows no obvious change in the labeled MSCs compared with the unlabeled MSCs (Figure S8B, Supporting Information). We further investigated the effect of TPSi NPs on osteocyte differentiation. As observed in Figure S9A in the Supporting Information, calcium deposits were observed in TPSi NP–labeled cells after 14 d of differentiation induction. Additionally, quantitative analysis via Alizarin Red staining showed similar levels of osteogenic differentiation between MSCs with and without TPSi NP labeling (Figure S9B, Supporting Information). Similarly, for the evaluation of chondrogenic differentiation, the trend for MSCs to differentiate into chondrocytes was not obviously affected by TPSi NP labeling (Figure S10A, Supporting Information). No obvious quantitative differences in the proportion of alcian blue–stained area were found between TPSi NP–labeled MSCs and unlabeled MSCs (Figure S10B, Supporting Information). Therefore, these data prove that TPSi NP labeling at concentrations less than 60 µg mL^{-1} exhibits feasible cytocompatibility and cannot adversely affect the multipotential differentiation of MSCs.
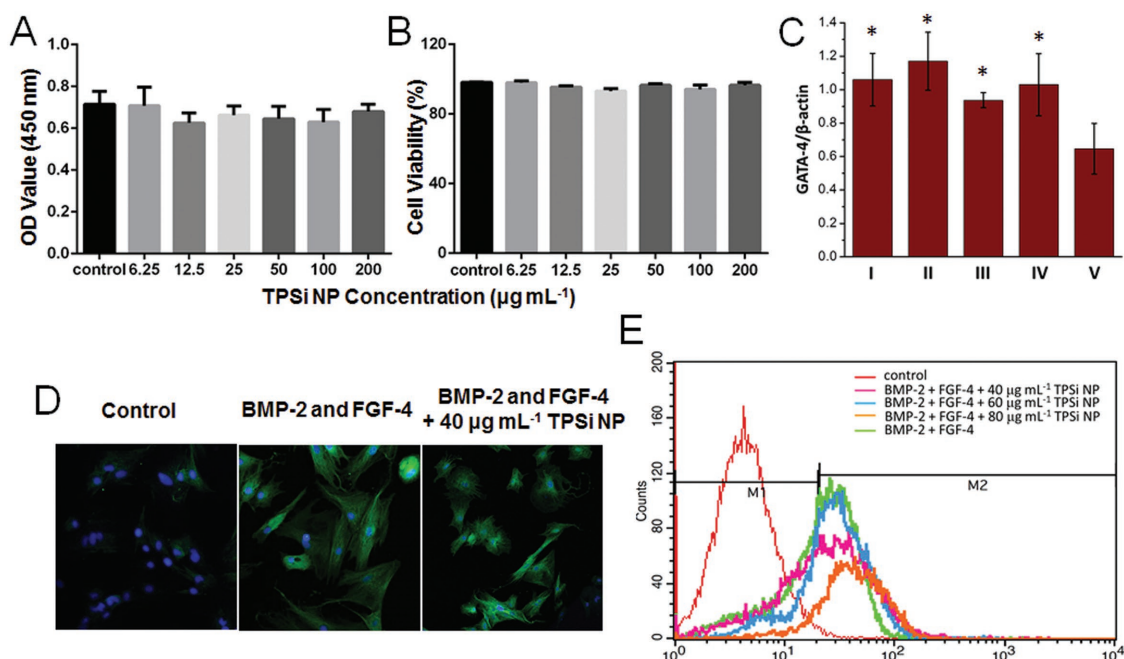
Figure 4. Effect of TPSi NP labeling on the cell survival of MSCs determined by the A) CCK-8 and B) LDH assays. C–E) Effect of TPSi NP labeling on the cardiomyocyte differentiation of MSCs. C) Quantification data of GATA-4 proteins in MSCs after induction with BMP-2 and FGF-4 in the presence of TPSi NPs at different concentrations by Western blot analysis (I: 40 μg mL^{-1}; II: 60 μg mL^{-1}; III: 80 μg mL^{-1}; IV: 0 μg mL^{-1}). V indicates the control group without induction. *Significant difference compared with the control group by one-way ANOVA analysis ($P < 0.05$). D) CLSM images showing the cTnI expression (green fluorescence) levels in MSCs without induction (left) and after BMP-2/FGF-4 induction in the absence (middle) and presence of 40 μg mL^{-1} TPSi NPs (right). E) Percentage of cTnI-positive cells in MSCs after BMP-2/FGF-4 induction in the presence of different concentrations of TPSi NPs determined by flow cytometry analysis.

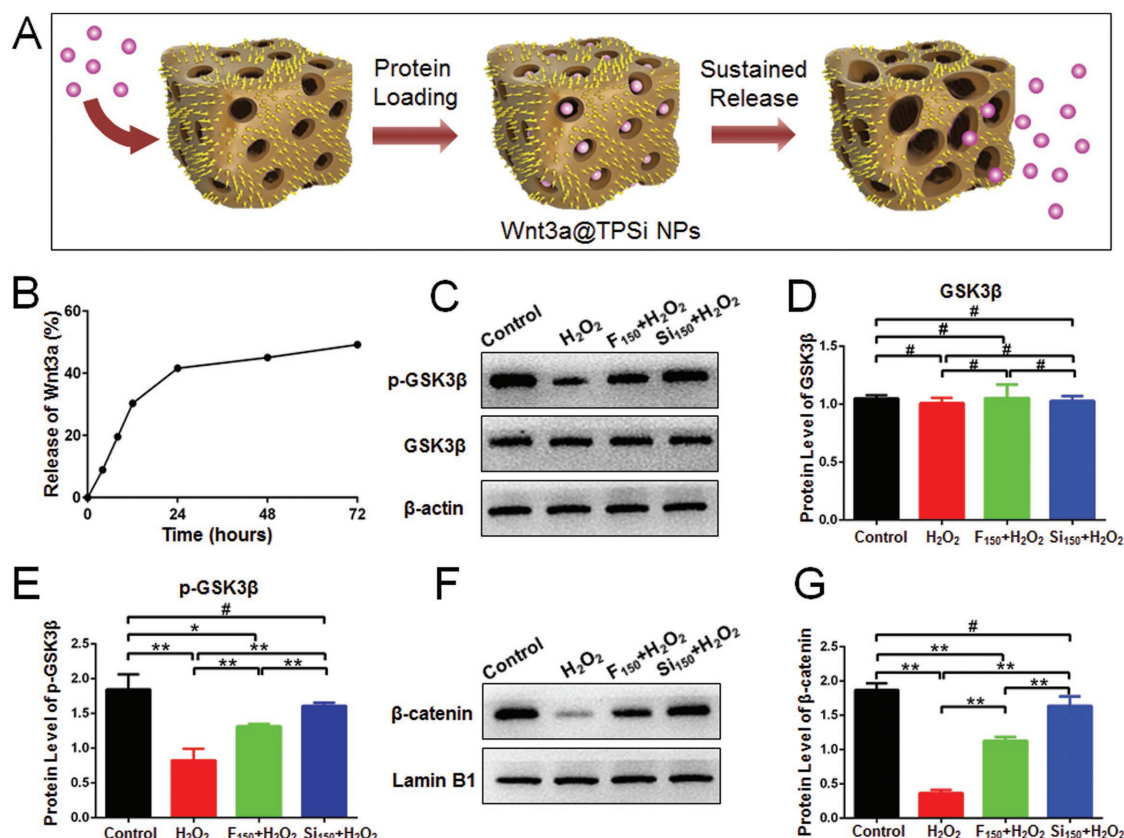## 2.5. Wnt3a Protein Loading and Sustained Release of Wnt3a@TPSi NPs

The involvement of Wnt/β-catenin signaling in numerous biological processes, including cell proliferation, antioxidative stress, and cardiac differentiation of MSCs, has been intensively investigated in recent years.[23] In particular, exogenous Wnt3a protein can attenuate β-catenin degradation and promote its nuclear localization by increasing the level of glycogen synthase kinase-3β (GSK-3β) phosphorylation. Therefore, it has been recognized as a potential protein drug for activating Wnt/β-catenin signaling. Unfortunately, the application of Wnt3a protein for stem cell protection is limited by its poor structural stability and dramatic aggregation in serum-free media.[24] Hence, an efficient strategy to enhance the bioavailability of Wnt3a protein is necessary to protect MSCs against oxidative damage. Silicon nanomaterial with suitable pore size is generally considered an efficient protective carrier for active proteins.[25] The loading process and sustained release behavior of Wnt3a protein in TPSi NPs are shown in **Figure 5**A. Wnt3a protein could be easily adsorbed in the porous framework of TPSi NPs, and the quantification result based on enzyme-linked immunosorbent assay (ELISA) showed that almost all the protein (the loading efficiency was calculated to be ≈98.1%) was successfully loaded in TPSi NPs by simple mixing of the protein and NPs at 4 °C for 1 h (Figure S11, Supporting Information). This high loading efficiency could be ascribed to suitable pore size, the large surface area of TPSi NPs, and their strong electrostatic interactions with the negatively charged Wnt3a protein. These features are

favorable not only for protein loading, but also for hindering its rapid release.[26] For release evaluation, a pellet of Wnt3a-loaded TPSi NPs was immersed in PBS with gentle shaking to mimic the normal physiological environment. As we anticipated, Figure 5B shows sustained release of Wnt3a that increases with time, i.e., release of ≈20% and 50% at 8 and 72 h, respectively.

2.6. Antioxidative Stress Effect and Mechanism of Wnt3a@TPSi NPs

The sustained release of Wnt3a proteins from TPSi NP is considered favorable for prolonging their activity in the absence of serum. To confirm this effect, we comparatively evaluated the abilities of Wnt3a in a free formulation and loaded in TPSi NPs to protect MSCs against oxidative stress in serum-free culture conditions. The MSCs were exposed to serum-free cell medium containing different concentrations of H$_2$O$_2$ in the range of 50×10^{-6} to 400×10^{-6} M for 24 h, and the cell viability was then measured via the CCK-8 assay to determine the effect of H$_2$O$_2$ concentration on the cell survival rate. Figure S12 in the Supporting Information indicates that the extent of oxidative damage induced by H$_2$O$_2$ increased significantly in a concentration-dependent manner. The H$_2$O$_2$ concentration of 100×10^{-6} M, which induces moderate cell damage, was chosen for this study to simulate the oxidative stress condition after myocardial damage.

The ability of free Wnt3a and Wnt3a-loaded TPSi NPs to influence canonical Wnt signaling under conditions with

**ADVANCED
SCIENCE NEWS**

www.advancedsciencenews.com

NANO · MICRO

small

www.small-journal.com

Figure 5. A) Schematic illustrations of the Wnt3a loading process and sustained release from TPSi NPs. B) The release curve of Wnt3a from TPSi NPs. Western blot bands and protein levels of C,E) p-GSK-3β, C,D) total GSK-3β, and F,G) β-catenin in H_2O_2-stimulated MSCs (denoted H_2O_2), free Wnt3a (C_{Wnt3a} = 150 ng mL^{-1})–treated/H_2O_2-stimulated MSCs (denoted $F_{150} + H_2O_2$), and Wnt3a@TPSi NP (C_{Wnt3a} = 150 ng mL^{-1})–labeled/H_2O_2-stimulated MSCs (denoted $Si_{150} + H_2O_2$). The concentration of TPSi NPs in group $Si_{150} + H_2O_2$ is about 6.1 µg mL^{-1}. $^{\#}P > 0.05$, $^{*}P < 0.05$, and $^{**}P < 0.01$ by the t-test.

H_2O_2 treatment was examined by quantifying changes in GSK-3β phosphorylation and nuclear β-catenin levels in MSCs (Figure 5C–G).[27] Western blot analysis revealed clear decreases in GSK-3β phosphorylation and nuclear β-catenin levels in MSCs upon H_2O_2 stimulation (Figure 5C,D). However, it was found that pretreatment of free Wnt3a or Wnt3a-loaded TPSi NPs with MSCs could inhibit the decline in GSK-3β phosphorylation induced by H_2O_2. More importantly, the GSK-3β in the MSCs labeled with Wnt3a-loaded TPSi NPs displayed a higher extent of phosphorylation than free Wnt3a. Additionally, increased nuclear localization of β-catenin was also observed in both Wnt3a-containing groups (Figure 5F,G). Notably, the level of β-catenin in the nuclear compartment was ≈45% higher for the Wnt3a-loaded TPSi NP group than the free Wnt3a group (Figure 5G). These results suggest the superior performance of Wnt3a-loaded TPSi NPs in promoting Wnt/β-catenin-dependent signaling.

Furthermore, quantification of the protein expression of both Bax and Bcl-2 in free Wnt3a– and Wnt3a@TPSi NP–treated MSCs after stimulation with H_2O_2 (100×10^{-6} M) for 24 h was carried out via Western blotting (**Figure 6**A,B). The ratio of Bax/Bcl-2 reflects the cell sensitivity to H_2O_2 stimuli, and a relatively lower Bax/Bcl-2 ratio indicates that MSCs are more resistant to oxidative stress than cells with a higher ratio.[28] As indicated in Figure 6B, the Bax/Bcl-2 ratio increased ≈5.30-fold in MSCs without Wnt3a after treatment with H_2O_2, suggesting their low resistance to oxidative stress. Nevertheless, a significant decrease in the Bax/Bcl-2 ratio was found for the two Wnt3a-treated groups compared with the MSC group without Wnt3a under oxidative stress conditions, which indicated the protective effect of Wnt3a treatment on MSCs. Importantly, compared with the free Wnt3a treatment (ratio of 1.03), the Wnt3a@TPSi NP labeling further decreased the Bax/Bcl-2 ratio (0.47) to the level similar to that of the group without H_2O_2 stimulation (0.41).

For further evaluation, the cell viability of each of the above groups was assessed using the CCK-8 assay. Figure 6C indicates that the cell viability of each Wnt3a-treated group treated with a Wnt3a concentration of 150 ng mL^{-1} was higher than that of the group treated with 50 ng mL^{-1}, initially revealing the dose-dependent enhancement of antioxidative stress ability. Notably, Wnt3a@TPSi NP labeling resulted in ≈27.2% and 25.0% higher cell viabilities than those of the free Wnt3a groups at concentrations of 50 and 150 ng mL^{-1}, respectively. As shown in Figure 6D, this enhancement effect was more evident when the MSCs were exposed to H_2O_2 for longer periods of time. For example, there was no significant difference in cell viability between the free Wnt3a and Wnt3a@TPSi NP groups
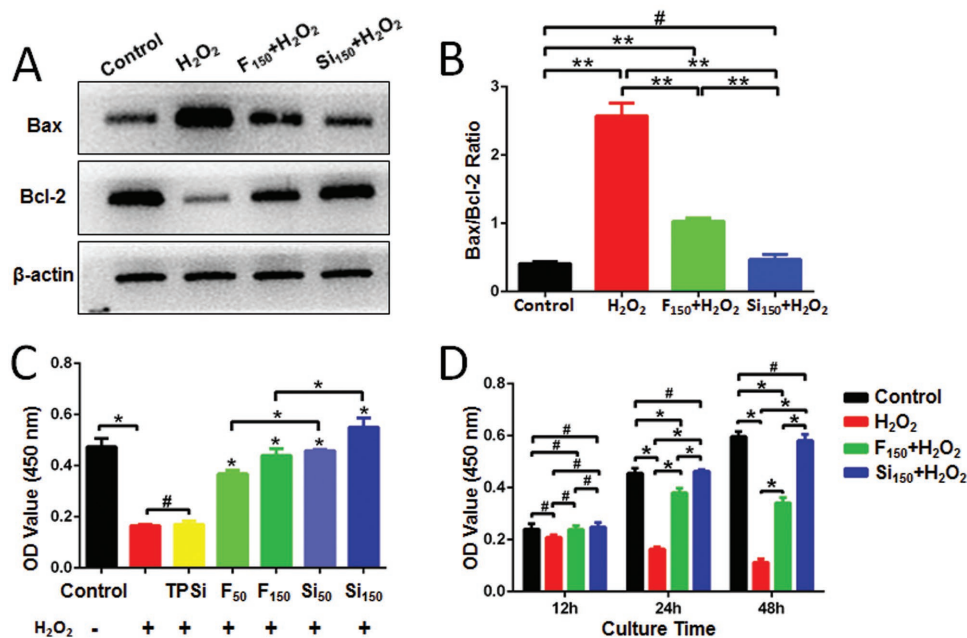
Figure 6. Antioxidative stress effect of free Wnt3a and Wnt3a@TPSi NPs in vitro. A,B) Western blot bands of the apoptosis-related proteins (Bax and Bcl-2) and the corresponding Bax/Bcl-2 ratios of the H_2O_2-stimulated MSCs (denoted H_2O_2), free Wnt3a ($C_{Wnt3a} = 150$ ng mL^{-1})–treated/H_2O_2-stimulated MSCs (denoted $F_{150} + H_2O_2$), and Wnt3a@TPSi NP ($C_{Wnt3a} = 150$ ng mL^{-1})–labeled/H_2O_2-stimulated MSCs (denoted $Si_{150} + H_2O_2$). C) Cell viabilities of different MSC groups after treatment with H_2O_2 for 24 h. Control: control group without H_2O_2 stimuli; H_2O_2: H_2O_2 treatment; TPSi: empty TPSi NPs ($C_{TPSi} = 6.1$ µg mL^{-1}); F_{50}: free Wnt3a ($C_{Wnt3a} = 50$ ng mL^{-1}); F_{150}: free Wnt3a ($C_{Wnt3a} = 150$ ng mL^{-1}); Si_{50}: labeling with Wnt3a@TPSi NPs ($C_{Wnt3a} = 50$ ng mL^{-1}); Si_{150}: labeling with Wnt3a@TPSi NPs ($C_{Wnt3a} = 150$ ng mL^{-1}). D) Cell viabilities of different MSC groups after treatment with H_2O_2 for different time periods (12, 24, and 48 h). $^{\#}P > 0.05$, $^*P < 0.05$, and $^{**}P < 0.01$ by the t-test.

(C_{Wnt3a}: 150 ng mL^{-1}) when the cells underwent H_2O_2 stimuli for only 12 h; however, the viability in the latter group increased as much as 70.3% compared to the viability in the former group after 48 h of H_2O_2 treatment, which may be attributed to the long-term maintenance of protein bioactivity in Wnt3a@TPSi NPs. Considering that oxidative stress generally exists in an infarcted myocardium for a long period of time,[29] the sustained cell protection effect through Wnt3a@TPSi NP labeling in MSCs will essentially promote cell survival and differentiation for optimal therapeutic effects.

2.7. US Imaging Capability

We also evaluated the in vitro echogenicity of the TPSi NP–labeled MSCs with a clinical scanner at a high frequency (22 MHz). After coincubation of MSCs with TPSi NPs at 40 µg mL^{-1} for 4 h, labeled MSCs (1×10^6 cells) were collected by centrifugation and resuspended in an agarose phantom with a volume of 0.25 mL. Additionally, the imaging signals of unlabeled MSCs with the same number of cells and a blank agarose phantom were also studied for comparison. As shown in **Figure 7**A–C, the B-mode image of TPSi NP–labeled MSCs was significantly brighter than that of the unlabeled MSCs. The quantitative result recorded by SONOMATH software revealed that compared to unlabeled MSCs, TPSi NP–labeled MSCs ($\approx$61.45 dB) exhibited $\approx$2.3-fold increase in US signal intensity (Figure 7D). This result indicates that the TPSi NPs performed well in US contrast imaging of the labeled MSCs.

We also studied contrast property of TPSi NPs alone in the agarose phantom. Only weak signal (2.73 dB) was observed in the phantom (Figure 7D). Therefore, the aggregation of TPSi NPs in the MSCs is the only possible reason for the significantly improved contrast.[10]

Furthermore, to understand how particle concentration affects the US signal, we imaged the cell samples at 30 MHz after subcutaneous injection of different numbers of TPSi NP–labeled MSCs into nude mice. As shown in Figure 7E, no obvious US signal was observed in the control group injected with PBS. However, the US signal of TPSi NP–labeled MSCs was immediately observed upon implantation when the cell number was above 5×10^4. Importantly, the average US signal intensity of TPSi NP–labeled MSCs is about 1.4-fold higher than that of unlabeled cells when the equivalent number (2×10^5) of MSCs were injected (Figure S13, Supporting Information). Furthermore, US images of different numbers of implanted TPSi NP–labeled MSCs demonstrated a cell number–dependent increase in echogenicity (Figure 7F).

2.8. In Vivo US-Enhanced Imaging after Intramyocardial Injection

Stem cell transplantation has shown great clinical potential as a primary or secondary therapeutic modality for a variety of diseases, particularly cardiac repair.[30] To improve the spatial accuracy of transplantation into myocardial tissue, stem cells are generally delivered by a combination of left thoracotomy

ADVANCED
SCIENCE NEWS
www.advancedsciencenews.com

NANO · MICRO
small
www.small-journal.com
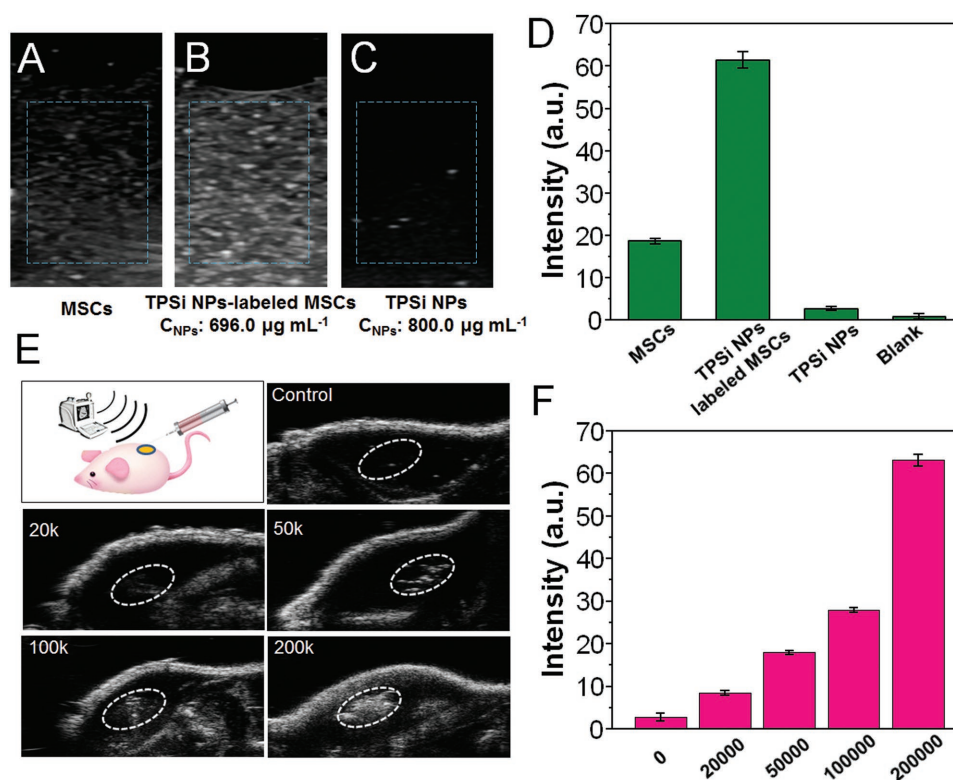
Figure 7. B-mode US images of agarose phantoms containing A) MSCs, B) TPSi NP–labeled MSCs, and C) TPSi NPs. D) The corresponding average US signal intensities of the above groups. E) US images and F) average US signal intensities of the subcutaneous tissues after injection with different numbers of labeled MSCs.

and sequential myocardial injection under direct visualization in many preclinical studies.[31] Unfortunately, the actual injection site is still not observed accurately with the current optical imaging techniques. Herein, to evaluate the US imaging performance of Wnt3a@TPSi NP–labeled MSCs in vivo, we separately injected equivalent numbers of labeled MSCs and unlabeled MSCs into the left ventricle wall of healthy nude mice. As shown in **Figure 8**A,B, there was no obvious US imaging signal change after the injection of unlabeled MSCs. In contrast, a sudden enhancement in imaging signal was clearly observed at the 0:17 time point for the labeled MSC group (Figure 8C,D; Movie S1, Supporting Information). Additionally, the enhanced region was located inside and fluctuated along with the ventricular wall, indicating precise injection of MSCs. More importantly, due to the enhanced effect of TPSi NPs, it was easy to ascertain the cell distribution by US imaging in the current stage. The statistical profile (Figure 8E,F) shows that the US intensity of the labeled MSC group increased by 2.2-fold compared to that of the unlabeled group. Overall, the above in vitro and in vivo studies both indicate that TPSi NP–mediated cellular labeling combined with US imaging guidance is a robust strategy for more precise MSC transplantation.

To investigate the safety of the local myocardial injection of the Wnt3a@PSi NP–labeled MSCs, we further carried out a complete blood panel, blood chemistry analysis, and hematoxylin and eosin (H&E) staining of the main organs of healthy Sprague-Dawley (SD) rats 30 d after implantation of the labeled MSCs (2×10^5 cells) in the left ventricle wall. SD rats treated

with the same number of unlabeled MSCs were evaluated as the control group. The hematological and blood test results of both MSC-treated groups exhibited no obvious difference from those of the untreated mice (Figure S14A–G, Supporting Information). Additionally, the histological examination of the heart, liver, spleen, lung, and kidney showed no noticeable damage, as observed by H&E-stained sections (Figure S15, Supporting Information), which means that the metabolites and degradation products from TPSi carriers are also nontoxic to the major organs. Overall, these results provide comprehensive evidence that the designed labeling nanoagent at the given dose can be safety administered in vivo.

3. Conclusion

We fabricated Wnt3a protein–loaded TPSi NPs as dual-functional US contrast/cell protection agents to label MSCs. This TAT-modified and PSi NP–based labeling agent was rapidly internalized by MSCs within 4 h and exhibited negligible effects on the survival and differentiation ability of MSCs. Such a nanosystem with a porous structure and capacity for intracellular degradability can carry Wnt3a proteins with high loading efficiency and release them in a sustained manner for antioxidative protection of the labeled MSCs. We also determined the sensitivity of TPSi NP labeling in US imaging of MSCs using both agarose phantom samples and in vivo mouse models. The results demonstrated that the intracellular particle aggregation
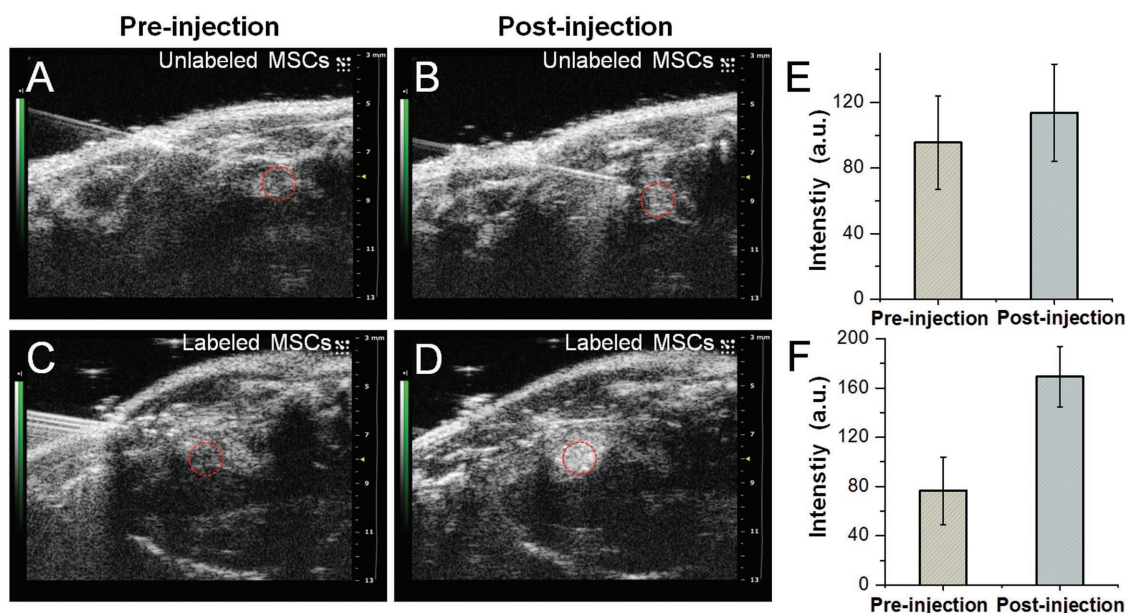
Figure 8. US images of the cardiac structure A,C) before and B,D) after intramyocardial injection of the A,B) unlabeled and C,D) Wnt3a@TPSi NP–labeled MSCs. Quantification of the US signal of the transplantation sites before and after MSC injection for the E) unlabeled and F) labeled groups. The average US intensity of the representative region indicated by the red circle was determined by the software SONOMATH.

of TPSi NPs could result in clear US signal amplification, which is anticipated to enable a considerable improvement in the precision of stem cell transplantation into the myocardium. It is considered that stem cell therapy in combination with a multifunctional TPSi NP–based theranostic strategy can be extended to wide applications, including myocardial infarction, ischemic stroke treatments, and cancer therapy, and has great potential for future clinical translation.

4. Experimental Section

Materials: TAT-FITC was purchased from Chinese Peptide Co., Ltd. *N*-Hydroxysuccinimide (NHS) and 1-ethyl-3-(3-dimethylaminopropyl) carbodiimide (EDC) were purchased from Sigma-Aldrich. BD Matrigel was used as a matrix for cell implantation. Low-glucose and high-glucose Dulbecco's modified Eagle's medium (LG-DMEM and HG-DMEM), fetal bovine serum (FBS), and penicillin + streptomycin were obtained from Gibco Company (USA). BMP-2 and FGF-4 were purchased from ATGen Company (BMP0905, USA) and Biolegend Company (592206, USA), respectively. Anti-cardiac troponin I polyclonal antibody (ab47003) and anti-GATA-4 monoclonal antibody (134057) and recombinant mouse Wnt3a protein were purchased from Abcam Company (UK). Fluorescent secondary antibody was obtained from Life Technology (1713763, USA).

Physical Characterizations: SEM images were obtained using a Hitachi S-4800 field-emission SEM. TEM images of material samples were acquired using a JEM-2100F electron microscope with an accelerating voltage of 200 kV. TEM images of cell samples were acquired using a JEM-1400 electron microscope with an accelerating voltage of 120 kV. The UV–vis spectra were obtained on a Shimadzu UV-3101PC UV–vis spectrophotometer. Fourier transform infrared spectroscopy analyses were conducted with a Nicolet 7000-C spectrometer. The element concentration in aqueous solution was measured by ICP-AES (Agilent). The porous characteristics of the material were evaluated using N_2 sorption at −196 °C using Tristar 3000 (Micromeritics Inc.). From the isotherm, the specific surface area was calculated using the Brunauer–Emmett–Teller theory and the total pore volume was estimated from the total adsorbed amount at a relative pressure of 0.97.

Preparation of TPSi NPs: Porous silicon multilayer films were first etched by pulsed electrochemical anodization of p-type (100) silicon wafers with a resistivity in the range of 0.01–0.02 Ω cm in a mixed 1:1 v/v aqueous electrolyte of HF (38%) and ethanol, as described previously.[15a] The multilayer film was lifted off from the substrate by increasing the anodization current into the electropolishing region. The PSi films were thermally carbonized with acetylene and then amine functionalized as described elsewhere.[32] Briefly, thermally carbonized PSi (TCPSi) films were immersed into HF to generate hydroxyl groups on the surfaces. The OH-terminated films were silanized using 10 vol% mixture of (3-aminopropyl)triethoxysilane (APTES) and anhydrous toluene for 1 h at room temperature. After washing the excess silane with toluene and ethanol, the films were dried for 16 h at 105 °C. The APTES-modified TCPSi films were then milled down into nanoparticles in a 5 vol% APTES–toluene solution using high-energy ball milling. After removal of the excess silane with fresh toluene and ethanol, the size selection of the amine-terminated PSi NPs was done with centrifugation.

TAT-FITC peptide (2 mg) was first dissolved in 2.0 mL of 2-(*N*-morpholino)ethanesulfonic acid buffer solution (pH 5.5). Then, 0.1 mmol of EDC and 0.25 mmol of NHS were sequentially added to the TAT solution to activate the carboxyl group of TAT. The mixture was stirred gently at room temperature for 1 h in the dark, and amine-modified PSi NPs (5 mg) in 5 mL of deionized water were then added. The above mixture was further stirred for 1 h at room temperature in the dark. The particles were washed with deionized water and collected by centrifugation at 14 000 rpm. The content of unbound TAT-FITC in washing solution was evaluated by UV–vis spectroscopy. Finally, the product was vacuum-dried or resuspended in PBS for further use. DLS measurements were conducted using a Zetasizer Nano analyzer (Malvern).

Cell Labeling Process: MSCs were cultivated in DMEM containing 10% v/v FBS, 100 units mL^{-1} penicillin, and 100 mg mL^{-1} streptomycin in a humidified incubator at 37 °C and 5% CO_2. To label the MSCs with TPSi NPs, TPSi NPs at different concentrations were added to the culture medium. After coincubation for 4 h, the MSCs were collected by cell dissociation and centrifugation at 1500 rpm. Then, the TPSi NP–labeled MSCs were suspended in a centrifuge tube for further biological characterization.

Material Degradation Evaluation: To evaluate the degradation behavior of TPSi NPs, the number of silicate ions leached from TPSi

**ADVANCED
SCIENCE NEWS**

www.advancedsciencenews.com

**NANO · MICRO
small**

www.small-journal.com

NPs was monitored by incubating the NPs in PBS at different pH values (8.4, 7.4, and 5.4) and measuring the Si concentration of the supernatant solution after centrifugation of the intact TPSi NPs. The pH value of the PBS solution was controlled by adding dilute hydrochloric acid or triethanolamine. The tubes containing the TPSi NP suspensions were placed on a shaking table at 140 rpm and 37 °C. Then, the Si concentration in the supernatant was measured by ICP-AES.

Furthermore, to observe the degradation behavior of TPSi NPs in MSCs, the TPSi NP–labeled MSCs were incubated in DMEM for different times (1, 8, and 16 d). The cells were detached, collected by centrifugation, and fixed with glutaraldehyde solution (2.5%). Then, the fixed cell sample was dehydrated with a graded ethanol series and propylene oxide, embedded in EPSM812, and polymerized at 37 °C for 12 h. Later, the ultrathin sections were cut by a diamond knife and observed by the JEM-1400 electron microscope.

Wnt3a Loading and the Release Curve of Wnt3a@TPSi NPs: 10 µg of recombinant mouse Wnt3a protein was added to sterile water for reconstitution to a concentration of 0.1 mg mL^{-1}. To load Wnt3a in TPSi NPs, 50 µL of the above Wnt3a solution was mixed with 200 µg of TPSi NPs in 100 µL of PBS (0.01×) for 1 h in a 4 °C ice bath by magnetic stirring. Then, the Wnt3a@TPSi NPs were collected by centrifugation at 10 000 rpm for 5 min. To analyze the Wnt3a loading efficiency, the supernatant was also collected after centrifugation of the above suspension, and the Wnt3a concentration was then measured using the Mouse Wnt3a ELISA Kit (Jianglai Biological Company, Shanghai, China).

To characterize the Wnt3a release behavior of Wnt3a@TPSi NPs, a certain mass of Wnt3a@TPSi NPs was suspended in 1 mL of sterile ultrapure water. Then, the plastic tube containing the above suspension was placed in a water bath shaker at 37 °C with moderate shaking at 80 rpm. A total of 100 µL of supernatant was collected at different time points (4, 8, 12, 24, 48, and 72 h) and centrifuged at 10 000 rpm for 5 min to remove the precipitate. The Wnt3a content in each supernatant was measured using an ELISA kit according to the manufacturer's instructions.

Evaluation of the Antioxidative Stress Effect of MSCs Labeled with Wnt3a@TPSi NPs In Vitro: The MSCs were seeded in 96-well plates at a density of 5×10^3 cells per well and cultured in DMEM containing 10% v/v FBS, 100 units mL^{-1} penicillin, and 100 mg mL^{-1} streptomycin for 12 h. Then, the cell medium was replaced with low-glucose cell medium containing 100 units mL^{-1} penicillin and 100 units mL^{-1} streptomycin and hydrogen peroxide at different concentrations (0, 50×10^{-6}, 100×10^{-6}, 200×10^{-6}, and 400×10^{-6} M). After further incubation for 24 h, the cell viability was evaluated using the CCK-8 assay. Finally, a H$_2$O$_2$ concentration of 100×10^{-6} M was chosen for further cell experiments.

To evaluate the antioxidative stress ability of MSCs labeled with Wnt3a@TPSi NPs, the cells were first incubated with different concentrations of Wnt3a protein in both the free Wnt3a form and the Wnt3a@TPSi NPs (the Wnt3a concentrations of two groups were 50 and 150 ng mL^{-1}, respectively) for 4 h in DMEM containing 10% v/v FBS, 100 units mL^{-1} penicillin, and 100 units mL^{-1} streptomycin. The cell medium was replaced with the above H$_2$O$_2$-containing/serum-free medium and cultured for another 24 h. After washing with PBS twice, cell viability was evaluated using the CCK-8 assay following the above procedure. Furthermore, the cell viability of the Wnt3a@TPSi NP–labeled MSCs (the Wnt3a concentration was 150 ng mL^{-1}) after culture in H$_2$O$_2$-containing/serum-free medium for different times (12, 24, and 48 h) was also evaluated.

To determine the protein levels (p-GSK-3β, GSK-3β, β-catenin, Bcl-2, and Bax) in free Wnt3a–treated and Wnt3a@TPSi NP–treated MSCs, MSCs (2×10^5 cells per well in six-well plates) were coincubated with each Wnt3a-containing sample for 4 h in DMEM before exposure to cell medium containing 100×10^{-6} M H$_2$O$_2$ for 24 h. Then, the protein in the MSCs was extracted by lysing the cells in lysis buffer. Furthermore, the nuclear protein was extracted by the NE-PER Nuclear and Cytoplasmic Extraction Kit (Thermo Fisher Scientific, USA) according to the manufacturer's instructions. The protein concentration was quantified via the BCA test (Thermo Fisher Scientific, USA). Later, the same amounts (25 µg) of the proteins were separated by means of a 10% polyacrylamide gel and transferred to polyvinylidene difluoride

membranes. The membranes were blocked with 5% skim milk, followed by incubation with different primary antibodies, including rabbit anti-mouse β-catenin (Proteintech, 1:500, 33 kDa), rabbit anti-mouse p-GSK-3β (Cell Signaling Technology, USA, 1:1000, 46 kDa), anti-mouse GSK-3β (Cell Signaling Technology, USA, 1:1000, 46 kDa), rabbit anti-mouse Bax (Cell Signaling Technology, USA, 1:1000, 20 kDa), mouse anti-mouse Bcl-2 (Novus, USA, 1:500, 24 kDa), mouse anti-mouse β-actin (Sigma, USA, 1:5000, 43 kDa), and rabbit anti-mouse lamin B1 (Proteintech, 1:500, 66 kDa) overnight at 4 °C. Then, the secondary antibody (goat anti-mouse immunoglobulin G or goat anti-rabbit immunoglobulin G, Cell Signaling Technology, USA) was added, and each membrane was incubated for an additional 2 h. Finally, the protein bands were visualized by an enhanced chemiluminescence detection kit (ECL, Thermo Fisher Scientific, USA) and exposed under a gel imaging system (Tanon 2500, Tanon Science & Technology Co., Ltd.). The expression of p-GSK-3 and total GSK-3 levels were detected in two different gels with the same loading quality of protein samples. The intensity of each band was measured by ImageJ software.

In Vitro Ultrasound Imaging: Different cell samples were dispersed in agarose to evaluate their in vitro US scattering signal. First, the labeled and unlabeled MSCs with the same number of cells (1×10^6 cells) were suspended in 0.25 mL of saline solution. At the same time, 1% agarose solution was obtained by adding agarose powder to deionized water, followed by heat treatment in a microwave oven for 2 min. Then, 0.25 mL of the cell suspension was mixed quickly with 0.25 mL of the agarose solution using a vortex mixer. Immediately, 0.25 mL of the mixed solution was added to the well of a 96-well plate. Additionally, the solidified 0.5% fresh agarose solution was also studied as a control group. The 96-well plate was placed under degassed water and scanned by the clinical US imaging system (GE Healthcare, mechanical index: 0.7, transducer frequency: 22 MHz). The US image of each sample was recorded, and the US intensity was read by the software SONOMATH (Ambition Co. Ltd., Chongqing, China). Three fields of view for each sample were collected to obtain the average intensity.

In Vivo US Imaging of Wnt3a@TPSi NP–Labeled MSCs in a Nude Mouse Model: The animal procedure followed the guidelines of the Institutional Animal Care and Use Committee at Tongji University. BALB/c nude mice (weight of ≈20 g) were purchased from Shanghai SLAC Laboratory Animal Co. Ltd. After coincubation of MSCs with Wnt3a@TPSi NPs at 40 µg mL^{-1} for 4 h, the labeled MSCs were detached from the culture dish and suspended in 1 mL of PBS. The cells were counted by a hemocytometer. Different numbers of labeled MSCs were resuspended in 200 µL of 1:1 PBS/Matrigel and injected subcutaneously into nude mice. The US image of each injected mouse was obtained under the VEVO LAZR imaging system (FUJIFILM VisualSonics, Inc., USA) at a frequency of 30 MHz. The US intensity of the region of interest was read by the software SONOMATH.

Furthermore, to evaluate the in vivo US imaging performance of the labeled MSCs applied via intramyocardial injection, 0.5 mL of Matrigel was mixed gently with 0.5 mL of PBS containing 2×10^6 labeled MSCs at 4 °C. Nude mice were anesthetized by isoflurane inhalation and fixed onto the operation platform. Then, 50 µL of the mixed solution was injected into the left ventricle wall of healthy nude mice for US imaging at a frequency of 30 MHz. The US images were recorded before and after injection of the sample.

Supporting Information

Supporting Information is available from the Wiley Online Library or from the author.

Conflict of Interest

The authors declare no conflict of interest.

Keywords

[1] a) V. F. M. Segers, R. T. Lee, *Nature* **2008**, *451*, 937; b) E. Gouadon, T. Moore-Morris, N. W. Smit, L. Chatenoud, R. Coronel, S. E. Harding, P. Jourdon, V. Lambert, C. Rucker-Martin, M. Puceat, *Stem Cells* **2016**, *34*, 34; c) Y. Li, D. L. Hermanson, B. S. Moriarity, D. S. Kaufman, *Cell Stem Cell* **2018**, *23*, 181; d) G. C. Chen, S. Y. Lin, D. H. Huang, Y. J. Zhang, C. Y. Li, M. Wang, Q. B. Wang, *Small* **2018**, *14*, 1702679; e) X. G. Li, T. Hamada, C. Ohata, M. Furumura, T. Hashimoto, *Exp. Dermatol.* **2013**, *22*, 515; f) R. Duelen, M. Sampaolesi, *EBioMedicine* **2017**, *16*, 30.

[2] P. K. Nguyen, J. Riegler, J. C. Wu, *Cell Stem Cell* **2014**, *14*, 431.

[3] a) K. M. Dean, A. E. Palmer, *Nat. Chem. Biol.* **2014**, *10*, 512; b) X. L. Qin, H. D. Chen, H. X. Yang, H. D. Wu, X. Zhao, H. Y. Wang, T. Chour, E. Neofytou, D. Ding, H. Daldrup-Link, S. C. Heilshorn, K. Li, J. C. Wu, *Adv. Funct. Mater.* **2018**, *28*, 1704939; c) E. M. Donnelly, K. P. Kubelick, D. S. Dumani, S. Y. Emelianov, *Nano Lett.* **2018**, *18*, 6625.

[4] E. G. Schutt, D. H. Klein, R. M. Mattrey, J. G. Riess, *Angew. Chem., Int. Ed.* **2003**, *42*, 3218.

[5] J. Lemaster, T. Kim, F. Chen, J. Jokerst, *ACS Appl. Nano Mater.* **2018**, *1*, 1321.

[6] N. H. Tsao, E. A. H. Hall, *Langmuir* **2016**, *32*, 6534.

[7] a) J. X. Wang, J. V. Jokerst, *Stem Cells Int.* **2016**, *5*, 9240652; b) P. J. Kempen, S. Greasley, K. A. Parker, J. L. Campbell, H. Y. Chang, J. R. Jones, R. Sinclair, S. S. Gambhir, J. V. Jokerst, *Theranostics* **2015**, *5*, 631; c) F. Foroutan, J. V. Jokerst, S. S. Gambhir, O. Vermesh, H. W. Kim, J. C. Knowles, *ACS Nano* **2015**, *9*, 1868.

[8] a) Q. F. Jin, C. Y. Lin, S. T. Kang, Y. C. Chang, H. R. Zheng, C. M. Yang, C. K. Yeh, *Ultrason. Sonochem.* **2017**, *36*, 262; b) A. Liberman, J. Wang, N. Lu, R. D. Viveros, C. A. Allen, R. F. Mattrey, S. L. Blair, W. C. Trogler, M. J. Kim, A. C. Kummel, *Adv. Funct. Mater.* **2015**, *25*, 4049; c) P. L. Lin, R. J. Eckersley, E. A. H. Hall, *Adv. Mater.* **2009**, *21*, 3949.

[9] K. Zhang, H. R. Chen, X. S. Guo, D. Zhang, Y. Y. Zheng, H. R. Zheng, J. L. Shi, *Sci. Rep.* **2015**, *5*, 8766.

[10] a) F. Chen, M. Ma, J. X. Wang, F. Wang, S. X. Chern, E. R. Zhao, A. Jhunjhunwala, S. Darmadi, H. R. Chen, J. V. Jokerst, *Nanoscale* **2017**, *9*, 402; b) J. V. Jokerst, C. Khademi, S. S. Gambhir, *Sci. Transl. Med.* **2013**, *5*, 177ra35.

[11] a) D. Shao, M. Q. Li, Z. Wang, X. Zheng, Y. H. Lao, Z. M. Chang, F. Zhang, M. M. Lu, J. Yue, H. Z. Hu, H. Z. Yan, L. Chen,

[12] S. Y. Liu, L. M. Tay, R. Anggara, Y. J. Chuah, Y. J. Kang, *ACS Appl. Mater. Interfaces* **2016**, *8*, 11925.

[13] E. Samper, A. Diez-Juan, J. A. Montero, P. Sepulveda, *Stem Cell Rev. Rep.* **2013**, *9*, 266.

[14] a) S. R. Yang, J. R. Park, K. S. Kang, *Oxid. Med. Cell. Longevity* **2015**, *1*, 486263; b) M. F. Pittenger, B. J. Martin, *Circ. Res.* **2004**, *95*, 9.

[15] a) L. M. Bimbo, M. Sarparanta, H. A. Santos, A. J. Airaksinen, E. Mäkilä, T. Laaksonen, L. Peltonen, V. P. Lehto, J. Hirvonen, J. Salonen, *ACS Nano* **2010**, *4*, 3023; b) D. J. Savage, X. W. Liu, S. A. Curley, M. Ferrari, R. E. Serda, *Curr. Opin. Pharmacol.* **2013**, *13*, 834; c) D. F. Liu, K. Lipponen, P. Quan, X. C. Wan, H. B. Zhan, E. Mäkilä, J. Salonen, R. Kostiainen, J. Hirvonen, T. Kotiaho, H. A. Santos, *ACS Biomater. Sci. Eng.* **2018**, *4*, 2308; d) L. A. Osminkina, A. A. Kudryavtsev, S. V. Zinovyev, A. P. Sviridov, Y. V. Kargina, K. P. Tamarov, V. N. Nikiforov, A. V. Ivanov, A. N. Vasilyev, V. Y. Timoshenko, *Bull. Exp. Biol. Med.* **2016**, *161*, 296; e) J. G. Croissant, Y. Fatieiev, N. M. Khashab, *Adv. Mater.* **2017**, *29*, 1604634; f) N. K. Hon, Z. Shaposhnik, E. D. Diebold, F. Tamanoi, B. Jalali, *J. Biomed. Mater. Res., Part A* **2012**, *100A*, 3416.

[16] a) H. A. Santos, E. Mäkilä, A. J. Airaksinen, L. M. Bimbo, J. Hirvonen, *Nanomedicine* **2014**, *9*, 535; b) J. S. Andrew, E. J. Anglin, E. C. Wu, M. Y. Chen, L. Y. Cheng, W. R. Freeman, M. J. Sailor, *Adv. Funct. Mater.* **2011**, *21*, 4410; c) W. Li, Z. H. Liu, F. Fontana, Y. P. Ding, D. F. Liu, J. T. Hirvonen, H. A. Santos, *Adv. Mater.* **2018**, *30*, 1703740; d) M. P. A. Ferreira, S. Ranjan, S. Kinnunen, A. Correia, V. Talman, E. Mäkilä, B. Barrios-Lopez, M. Kemell, V. Balasubramanian, J. Salonen, J. Hirvonen, H. Ruskoaho, A. J. Airaksinen, H. A. Santos, *Small* **2017**, *13*, 1701276; e) M. P. A. Ferreira, S. Ranjan, A. M. R. Correia, E. M. Mäkilä, S. M. Kinnunen, H. B. Zhang, M. A. Shahbazi, P. V. Almeida, J. J. Salonen, H. J. Ruskoaho, A. J. Airaksinen, J. T. Hirvonen, H. A. Santos, *Biomaterials* **2016**, *94*, 93.

[17] Y. Lei, H. Tang, L. Yao, R. Yu, M. Feng, B. Zou, *Bioconjugate Chem.* **2008**, *19*, 421.

[18] E. M. Kawamoto, M. Gleichmann, L. M. Yshii, L. D. Lima, M. P. Mattson, C. Scavone, *Braz. J. Med. Biol. Res.* **2012**, *45*, 58.

[19] L. M. Pan, Q. J. He, J. N. Liu, Y. Chen, M. Ma, L. L. Zhang, J. L. Shi, *J. Am. Chem. Soc.* **2012**, *134*, 5722.

[20] a) S. H. C. Anderson, H. Elliott, D. J. Wallis, L. T. Canham, J. J. Powell, *Phys. Status Solidi A* **2003**, *197*, 331; b) M. Ariza-Avidad, A. Nieto, A. Salinas-Castillo, L. F. Capitan-Vallvey, G. M. Miskelly, M. J. Sailor, *Nanoscale Res. Lett.* **2014**, *9*, 410.

[21] A. Uccelli, L. Moretta, V. Pistoia, *Nat. Rev. Immunol.* **2008**, *8*, 726.

[22] a) P. M. Ku, L. J. Chen, J. R. Liang, K. C. Cheng, Y. X. Li, J. T. Cheng, *Cardiovasc. Diabetol.* **2011**, *10*, 57; b) J. Yoon, B. G. Min, Y. H. Kim, W. J. Shim, Y. M. Ro, D. S. Lim, *Acta Cardiol.* **2005**, *60*, 277.

[23] a) K. Willert, J. D. Brown, E. Danenberg, A. W. Duncan, I. L. Weissman, T. Reya, J. R. Yates, R. Nusse, *Nature* **2003**, *423*, 448; b) G. Ozhan, G. Weidinger, *Cell Regener.* **2015**, *4*, 3.

[24] N. Tuysuz, L. van Blooi, S. van den Brink, H. Begthel, M. M. A. Verstegen, L. J. Cruz, L. J. Hui, L. J. W. van der Laan, J. de Jonge, R. Vries, E. Braakman, E. Mastrobattista, J. J. Cornelissen, H. Clevers, D. ten Berge, *Nat. Commun.* **2017**, *8*, 14578.

[25] a) H. A. Santos, J. Hirvonen, *Nanomedicine* **2012**, *7*, 1281; b) D. F. Liu, E. Mäkilä, H. B. Zhang, B. Herranz, M. Kaasalainen, P. Kinnari, J. Salonen, J. Hirvonen, H. A. Santos, *Adv. Funct. Mater.* **2013**, *23*, 1893; c) M. P. A. Ferreira, V. Talman, G. Torrieri, D. F. Liu, G. Marques, K. Moslova, Z. H. Liu, J. F. Pinto, J. Hirvonen, H. Ruskoaho, H. A. Santos, *Adv. Funct. Mater.* **2018**, *28*,

1705134; d) M. A. Tolli, M. P. A. Ferreira, S. M. Kinnunen, J. Rysa, E. M. Mäkilä, Z. Szabo, R. E. Serpi, P. J. Ohukainen, M. J. Valimaki, A. M. R. Correia, J. J. Salonen, J. T. Hirvonen, H. J. Ruskoaho, H. A. Santos, *Biomaterials* **2014**, *35*, 8394.

[26] M. Kaasalainen, J. Rytkonen, E. Mäkilä, A. Narvanen, J. Salonen, *Langmuir* **2015**, *31*, 1722.

[27] J. G. Kim, M. J. Kim, W. J. Choi, M. Y. Moon, H. J. Kim, J. Y. Lee, J. Kim, S. C. Kim, S. G. Kang, G. Y. Seo, P. H. Kim, J. B. Park, *J. Cell. Physiol.* **2017**, *232*, 1104.

[28] M. Raisova, A. M. Hossini, J. Eberle, C. Riebeling, T. Wieder, I. Sturm, P. T. Daniel, C. E. Orfanos, C. C. Geilen, *J. Invest. Dermatol.* **2001**, *117*, 333.

[29] O. C. Bezerra, C. M. Franca, J. A. Rocha, G. A. Neves, P. R. M. Souza, M. T. Gomes, C. Malfitano, T. C. A. Loleiro, P. M. Dourado, S. Llesuy, K. de Angelis, M. C. C. Irigoyen, L. Ulloa, F. M. Consolim-Colombo, *Sci. Rep.* **2017**, *7*, 13687.

[30] a) H. K. Haider, M. Ashraf, *Am. J. Physiol.: Heart Circ. Physiol.* **2005**, *288*, H2557; b) E. Cambria, F. S. Pasqualini, P. Wolint, J. Gunter, J. Steiger, A. Bopp, S. P. Hoerstrup, M. Y. Emmert, *npj Regener. Med.* **2017**, *2*, 17.

[31] C. C. Sheng, L. Zhou, J. J. Hao, *BioMed. Res. Int.* **2013**, *2013*, 547902.

[32] E. Mäkilä, L. M. Bimbo, M. Kaasalainen, B. Herranz, A. J. Airaksinen, M. Heinonen, E. Kukk, J. Hirvonen, H. A. Santos, J. Salonen, *Langmuir* **2012**, *28*, 14045.

1804332 (13 of 13)